
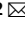






# A portable scanner for magnetic resonance imaging of the brain

Clarissa Z. Cooley<sup>1,2</sup>  , Patrick C. McDaniel<sup>1,3</sup>, Jason P. Stockmann<sup>1,2</sup>, Sai Abitha Srinivas<sup>1</sup>, Stephen F. Cauley<sup>1,2</sup>, Monika Śliwiak<sup>1</sup>, Charlotte R. Sappo<sup>1</sup>, Christopher F. Vaughn<sup>1</sup>, Bastien Guerin<sup>1,2</sup>, Matthew S. Rosen<sup>1,2,4</sup> , Michael H. Lev<sup>1,2,5</sup>  and Lawrence L. Wald<sup>1,2,6</sup>

**Access to scanners for magnetic resonance imaging (MRI) is typically limited by cost and by infrastructure requirements. Here, we report the design and testing of a portable prototype scanner for brain MRI that uses a compact and lightweight permanent rare-earth magnet with a built-in readout field gradient. The 122-kg low-field (80 mT) magnet has a Halbach cylinder design that results in a minimal stray field and requires neither cryogenics nor external power. The built-in magnetic field gradient reduces the reliance on high-power gradient drivers, lowering the overall requirements for power and cooling, and reducing acoustic noise. Imperfections in the encoding fields are mitigated with a generalized iterative image reconstruction technique that leverages previous characterization of the field patterns. In healthy adult volunteers, the scanner can generate T1-weighted, T2-weighted and proton density-weighted brain images with a spatial resolution of  $2.2 \times 1.3 \times 6.8 \text{ mm}^3$ . Future versions of the scanner could improve the accessibility of brain MRI at the point of care, particularly for critically ill patients.**

Neurological disorders are the second leading cause of death and the leading cause of disability globally<sup>1</sup>. Magnetic resonance imaging (MRI) is the reference standard for assessment of these disorders due to its ability to image intracranial anatomy with unparalleled soft tissue contrast. However, large populations of patients are precluded from access to MRI due to its limitations. Most notably, MRI scanners are costly, require special infrastructure and are immobile. This makes MRI unavailable to patients who cannot be safely transported to the scanner or who are in low-resource settings.

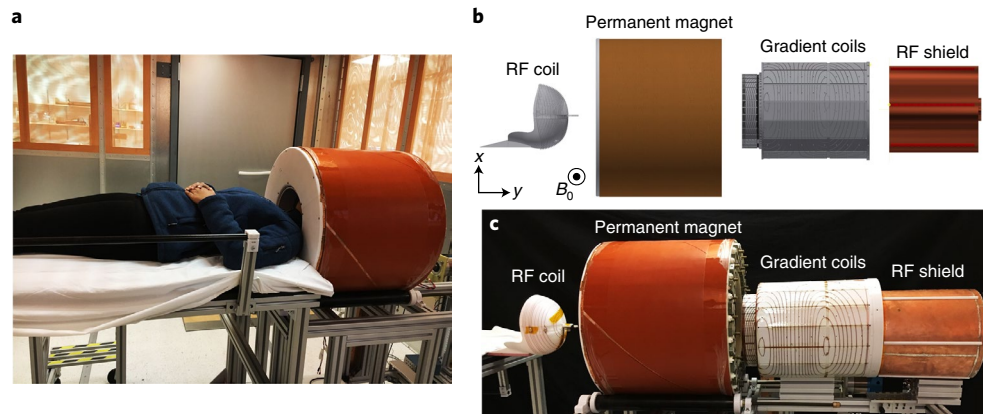
The development of a portable, low-cost MRI device for brain imaging could expand access to MRI neuroimaging and enable point-of-care (POC) diagnostics. In emergency medicine, neuroimaging constitutes the majority of MRI examinations<sup>2</sup>. POC MRI could expedite assessment of neurological emergencies that are not as accurately characterized by computed tomography. For example, POC MRI could detect subtle signs of increased intracranial pressure associated with head trauma, stroke, haematomas or hydrocephalus. Similar needs exist for critically ill patients in neurological intensive care units. It can be difficult or unsafe to transport these unstable patients to a fixed MRI scanner, which might even be located in a different building<sup>3</sup>. Neonatal imaging introduces related logistical burdens<sup>4</sup> that could be addressed with a POC bedside MRI scanner. Finally, accessible, low-cost MRI could benefit remote low- and middle-income regions both in the United States and elsewhere; for example, in monitoring the treatment of paediatric hydrocephalus in sub-Saharan Africa<sup>5</sup>. Overall, a portable MRI head scanner capable of cost-efficient operation outside a central radiology department could improve patient outcomes by detecting time-critical pathology and informing immediate clinical management at the POC.

The design for conventional MRI scanners is fundamentally unsuitable for POC operation. The cost and size of conventional

scanners result from their reliance on high-strength, homogeneous, static magnetic fields and switchable linear field gradients<sup>6</sup>. In traditional design, high magnetic fields (static polarizing field ( $B_0$ )  $> 1.5 \text{ T}$ ) are desirable to increase detection sensitivity while high magnetic homogeneity is needed to ensure that the magnetic resonance image is encoded exclusively by the switchable field gradients. Based on these principles, conventional MRI scanner design has converged on a large superconducting magnet (4–10 tonnes) requiring high-cost and maintenance-intensive cryogenic components. The switching linear gradient fields are the primary source of acoustic noise ( $> 130 \text{ dB}$ ) and use of power (up to 1,000 A and 2 kV), and require water cooling. This combination results in expensive, large, heavy scanners that must be sited in a dedicated suite with special power and cooling services. The complex and potentially dangerous hardware requires highly trained staff to run and maintain the equipment and a safety exclusion zone to prevent projectile accidents with ferrous objects. These aspects contribute to the relative sparsity of MRI scanners compared with other imaging tools, including digital X-ray (DXR), computed tomography and ultrasound—less expensive systems that can be used in a wider variety of settings. Furthermore, there is a large global disparity in MRI scanner density related to income levels and infrastructure<sup>7</sup>.

The need for lower-cost and simplified siting of brain scanners has been recognized by the MRI community and has driven recent industrial efforts. These include the assessment of a 0.55-T whole-body superconducting system<sup>8</sup> and the development of a compact superconducting 3-T brain scanner<sup>9</sup>, a small-footprint, cryogen-free 0.5-T head scanner (<https://www.synaptivemedical.com/products/evry/>), a 1-T permanent magnet system for siting in the neonatal intensive care unit (<https://www.aspectimaging.com/>), a low-field system for dedicated prostate imaging and biopsy guidance (<https://promaxo.com/>) and a 64-mT portable

<sup>1</sup>Athinoula A. Martinos Center for Biomedical Imaging, Department of Radiology, Massachusetts General Hospital, Charlestown, MA, USA. <sup>2</sup>Harvard Medical School, Boston, MA, USA. <sup>3</sup>Department of Electrical Engineering and Computer Science, Massachusetts Institute of Technology, Cambridge, MA, USA. <sup>4</sup>Department of Physics, Harvard University, Cambridge, MA, USA. <sup>5</sup>Department of Radiology, Massachusetts General Hospital, Boston, MA, USA. <sup>6</sup>Harvard-MIT Division of Health Sciences and Technology, Cambridge, MA, USA. ✉e-mail: [czcooley@mgh.harvard.edu](mailto:czcooley@mgh.harvard.edu)



**Fig. 1 | Portable MRI brain scanner prototype.** **a**, The scanner's main components are inside the 56-cm-diameter magnet (orange cylinder). The amplifier console and computer are not shown. The participant's shoulders remain outside the magnet, allowing for a lightweight, small bore design that fits the head only. The patient table detaches from the scanner cart to facilitate transport. **b**, Exploded computer-aided design (CAD) model of the main scanner components (from left to right): the spiral transmit/receive RF helmet coil; the Halbach magnet cylinder; the two-axis gradient coil; and the RF shield. **c**, Photograph corresponding to the exploded view in **b**.

brain scanner (<https://www.hyperfine.io/portable-mri>). In addition to these industrial initiatives, there are academic efforts directed towards more accessible MRI. Low-cost pre-polarized systems have been developed for extremity<sup>10</sup> and brain<sup>11</sup> imaging; the brain imager employed cryogenic superconducting quantum interference device (SQUID) detectors, a 0.1-T pre-polarizing field and an ultra-low readout field (0.2 mT). Brain imaging has also been shown in a low-cost, 6.5-mT scanner without pre-polarization and cryogenics, instead focusing on high data-rate image encoding and advanced reconstruction methods<sup>12</sup>. Although these ultra-low-field brain scanners are low cost, they are not portable, and the image quality is limited by a poor signal-to-noise ratio (SNR) at the ultra-low field strength. A high-field brain scanner has been proposed with a head-only, high-temperature, superconducting magnet<sup>13</sup>. While compact and easily site-able, this design is not intended for truly portable applications given the size of its magnetic footprint and cryogenic requirements. Arrays of permanent magnets have been proposed for low-field portable brain scanners<sup>14–17</sup>. This method is compelling because permanent magnets do not require power or cooling, and the low-field architecture can be configured to have a minimal external magnetic footprint, reducing safety concerns from potential introduced ferrous objects in POC use.

Despite the rapid progress and growing interest in the field, there is no consensus on the best approach for adapting MRI to portable and POC use. To significantly reduce the size, cost and complexity of the hardware, our design departs from the canonical scanner design (that is,  $B_0$  field homogeneity plus three switchable linear gradients). Our approach is summarized by four points. First, instead of a versatile, full-body diagnostic device, we focus on a specialized portable design for brain imaging. The small size of the head relative to the torso lends itself naturally to scanner size reduction, facilitating a small-diameter, short bore design that fits around the head only. Second, we use a low-field magnet consisting of an optimized array of rare-earth material to generate the static  $B_0$  field. The use of permanent magnets capitalizes on the stored magnetic field of these alloys, obviating the need for cryogenics and external current sources. In contrast with the severe SNR penalty at ultra-low field, a low-field magnet in the 50–200 mT range provides a workable trade-off between the SNR, safety, cost and footprint required for POC applications. Third, rather than designing the  $B_0$  magnet to be homogeneous, we build in spatial field variation for image encoding. This allows a reduction in magnet size, and it eliminates the need for a traditional readout gradient electromagnetic system, reducing the acoustic noise, power and cooling requirements of the

scanner. Finally, we leverage Moore's law<sup>18</sup> by relaxing hardware constraints and addressing the resulting issues with advanced image reconstruction methods, effectively shifting the burden from hardware to software.

Although the sensitivity of the proposed POC scanner is close to that of low-field clinical scanners, high-field MRI offers superior image quality and more advanced imaging techniques (for example, spectroscopy, susceptibility weighted imaging and diffusion tensor imaging). The proposed device is therefore not intended to replace high-field MRI scanners, but rather to offer useful MRI diagnostics to populations for whom examination with a conventional, fixed MRI scanner is impractical or impossible, as well as for whom other available imaging modalities, such as ultrasound, provide only limited or suboptimal clinical assessment.

Here, we present the design and validation of the head-only, portable, lightweight, low-field (80 mT) MRI scanner based on a compact permanent magnet array that weighs only 122 kg. Our scanner operates from a standard wall outlet, requires no cooling and can be mounted on a cart or within an ambulance or van for transportation to the POC. We present the overall scanner and subsystem design, the imaging sequence and reconstruction approach and in vivo brain imaging validation (acquired in a radiofrequency (RF) shielded room) using T1, T2 and proton density-weighted imaging.

**Prototype scanner.** Figure 1 shows the compact POC scanner located in an RF shielded room with a human participant in position for scanning, as well as an exploded view of the in-bore scanner components. From left to right, these are: the 12-turn single-channel RF transmit/receive coil helmet; the permanent magnet cylinder; the gradient coils; and the RF shield. The total estimated weight of the full scanner system (including the magnet, coils, amplifiers, console and cart) is 230 kg. The cart can be pushed by a single person for transport. If the currently used general-purpose prototyping equipment (console, amplifiers and cart) is replaced with custom efficient lightweight designs, we project a total scanner weight of ~160 kg.

**Permanent magnet.** The head-only permanent magnet consists of a sparse array of neodymium (NdFeB) rare-earth magnets in a Halbach cylinder configuration<sup>14,19</sup>. The Halbach cylinder's  $B_0$  direction is transverse to the axis of the cylinder. We define the  $B_0$  direction as the  $z$  direction and label the  $y$  direction along the cylinder axis. The ideal dipolar Halbach configuration consists of permanent magnet segments with a magnetization direction that

rotates  $4\pi$  around the cylinder azimuthally<sup>20</sup>. This results in a homogeneous transverse field inside the magnet and zero field outside the magnet. The intrinsically self-shielding design is ideal for portable applications where stray fields pose operational and safety hazards. In addition, unlike other permanent magnet designs, the Halbach magnet does not require a heavy, high-permeability (iron/steel) yoke to guide the flux lines, yielding an efficient strength-to-weight ratio. There is an inherent trade-off between a magnet's size and homogeneity in the imaging region of interest (ROI). For a given volume of permanent magnet material, there is also a trade-off between the diameter of the magnet and the field strength. To maintain a small magnet diameter (for portability and field strength), we design the magnet for operation with the participant's shoulders outside the magnet.

In practice, a highly homogeneous Halbach magnet with these geometric constraints is difficult to achieve. Instead of striving to maximize homogeneity in our design, the magnetic field variation is shaped into a built-in field gradient for image encoding. This approach allows a very compact, intrinsically inhomogeneous, lightweight magnet and eliminates the need for one of the three gradient coil systems. Specifically, the built-in gradient replaces the readout gradient system (coil + current driver), which would normally need to overcome the magnet's spurious  $B_0$  variation. This would require high power and cooling for conventional encoding approaches within the inhomogeneous magnet. The high-power readout gradient would also produce high acoustic noise during switching. Overall, the built-in gradient design is attractive for a POC scanner as it reduces the magnet cost and size and significantly reduces the full system's power/cooling needs and acoustic noise. However, we note that this scheme reduces flexibility in the choice of pulse sequences.

We allowed a genetic optimization algorithm to perturb the basic Halbach cylinder design by placing two grades (N42 and N52) of 1'' NdFeB permanent magnet cubes to produce a favourable  $B_0$  field and built-in gradient in the  $x$  direction<sup>14</sup> (the coordinate system was changed compared with previous publications<sup>14,19,21–23</sup>, to adhere to the more traditional use of  $x$  for the readout gradient direction). Figure 2 shows the resulting magnet design with 641 NdFeB 1'' cubes arranged in three layers of 24 rungs. Figure 2a,b shows photographs of the superior end of the magnet with the cover removed, exposing the ends of the magnet rungs and shim trays (the single-row third layer near the shoulders is not visible). The NdFeB cubes are contained within the green, square cross-section, structural fibreglass tubes. Figure 2c,d shows the optimized arrangement of N42 (white) and N52 (grey) magnets and the measured  $B_0$  field maps. To improve the gradient field shape, a second optimization stage followed for shim magnet placement with smaller NdFeB elements<sup>23</sup> (visualized in Fig. 2e), using a similar algorithm. Figure 2f shows the improved gradient linearity after shimming. Compared with the orientation of the field maps shown in Fig. 2, for the imaging experiments, the magnet was rotated by  $60^\circ$  to help minimize nonlinearities in the field of view (FOV).

The constructed magnet assembly has a length of 49 cm, an outer diameter of 57 cm, an inner diameter of 35 cm and a bore access diameter at the shoulders of 27 cm. The magnet uses 80 kg of NdFeB material and the constructed assembly weight is 122 kg. The  $B_0$  field averages 80 mT over the target 20-cm-diameter spherical volume and contains a built-in readout gradient of  $7.6\text{ mT m}^{-1}$ . On average, the pull force on a ferrous object equals its weight at  $\sim 13\text{ cm}$  from the bore opening and  $\sim 1\text{ cm}$  from the outer cylindrical surface, demonstrating a considerably smaller safety footprint than conventional high-field MRI magnets.

**Gradient coils.** While the magnet's built-in field variation is used for image encoding in the  $x$  dimension, we used the switchable gradient coils shown in Fig. 3 for phase encoding in the  $y$  and  $z$  directions. Previously, we introduced alternative encoding methods that

further reduced the need for switchable gradient systems, specifically the combination of generalized projection imaging by rotating the Halbach magnet<sup>19,22</sup> and either a phase-encode gradient coil or RF encoding method, such as transmit array spatial encoding<sup>21</sup>, for encoding along the axis of the cylinder. While these methods can further reduce or eliminate the need for gradient power amplifiers (GPAs), they also require additional hardware. Moreover, the use of switchable gradients for phase encoding within a spin-echo sequence proved more robust to image artefacts. Although we employ switchable gradients to encode in two directions ( $y$  and  $z$ ), minimal power is needed compared with conventional scanners. The power reduction arises from two sources. First, unlike the readout gradient, phase-encoding gradients need not dominate the  $B_0$  inhomogeneity ( $\Delta B_0$ ) in a spin-echo sequence since the  $\Delta B_0$  phase dispersion is refocused in the spin echo. Second, the permanent magnet design supports the use of efficient gradient coils. The gradient coil efficiency benefits from the compact, head-only geometry as well as the lack of shielding windings. This shielding layer is conventionally needed to prevent eddy currents on the conductive components of the superconducting magnet and cryostat. However, the NdFeB magnets are made from sintered material that does not support significant induced eddy currents, eliminating the need for the shielding layer (and thus improving gradient efficiency). In the imaging experiments described here, peak currents of 9 and 4.5 A were used to drive the  $z$  and  $y$  gradient, respectively.

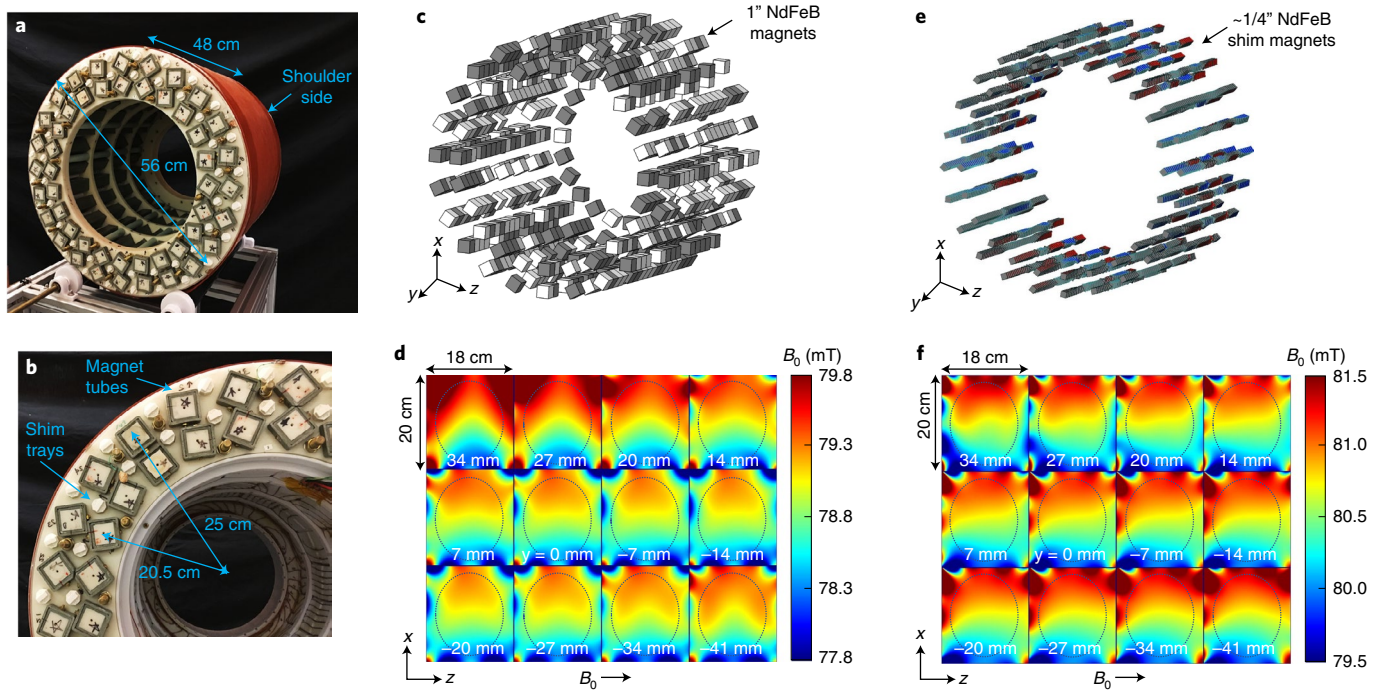
Acoustic noise from gradient switching is much lower in this scanner compared with conventional MRI scanners due to the lower  $B_0$  field and elimination of the readout gradient coil. The A-weighted peak and average sound pressure levels measured at the magnet centre during the rapid acquisition and relaxation enhancement (RARE) sequence were 75.4 and 69.3 dB, respectively, using a Bruel and Kjaer model 2238 Mediator SPL meter with the manufacturer's microphone and extension cable.

**Sequences.** The low  $B_0$  field and built-in gradient pose unique MRI spin manipulation problems and sequence considerations. Because the RF frequencies of the transmit ( $B_1+$ ) and receive ( $B_1-$ ) magnetic fields are proportional to the inhomogeneous  $B_0$  field, the 20-cm ROI encapsulates a Larmor range of 3.35–3.43 MHz (80 KHz bandwidth). Traditional hard  $B_1+$  pulses would require high RF power levels to manipulate all of the spins in the wide Larmor frequency bandwidth. Instead, we employ frequency-swept chirped  $B_1+$  pulses for excitation and refocusing, which cover a large bandwidth and are less susceptible to  $B_1+$  amplitude variation<sup>21,24</sup>.

The built-in gradient precludes the standard formation of a gradient echo and thus limits the MRI acquisition method to spin-echo-based sequences. Compared with high-field MRI, the lower  $B_0$  field leads to low RF heating and longer spin coherence times ( $T_2$  relaxation times). We take advantage of these properties to enable an efficient acquisition sequence using long multi-echo RARE<sup>25</sup> volumetric spin-echo sequences (Fig. 4). While we demonstrate a three-dimensional (3D) encoding approach utilizing the built-in gradient as a readout gradient, it is also possible to use the gradient as a slice-selection gradient for two-dimensional (2D) imaging with phase encoding for in-plane encoding<sup>26,27</sup>.

**Image reconstruction.** Traditional MRI image reconstruction relies on the use of linear encoding fields to reconstruct  $k$ -space data using the fast Fourier transform (FFT) algorithm. Although we optimized the gradient-encoding fields for linearity, the compact nature of the system limits linearity in the ROI, particularly towards the periphery of the permanent magnet gradient,  $G_x$ . Nonlinear encoding fields can lead to image aliasing and encoding holes<sup>19,28,29</sup>, which can sometimes be alleviated with the use of multi-coil receive arrays. However, if the encoding fields are monotonic, the nonlinearities will translate to more benign geometric distortion





**Fig. 2 | Permanent low-field magnet design.** **a**, The  $B_0 = 80$  mT cylindrical Halbach magnet has an outer diameter of 56 cm, a length of 48 cm and a total weight of 122 kg (80 kg of rare-earth material). The photograph shows the superior side (service end) of the magnet with a 35.3-cm-diameter opening. The inferior side of the magnet (shoulder side) has a 27-cm bore opening due to the 32-cm-diameter ring of 1" booster magnets near the shoulders, placed to alleviate the field fall-off. **b**, Close-up photograph of the superior end of the magnet. The 1" NdFeB magnets are contained within the square cross-section fibreglass tubes. The two main magnet layers are at radii of 20.5 and 25 cm. The white plastic shim trays contain the addition of smaller NdFeB magnets to further optimize the magnet field. **c**, CAD model showing the distribution of N52 grade (grey) and N42 grade (white) NdFeB 1" cubes comprising the Halbach magnet, optimized for a built-in monotonic readout encoding field in the  $x$  direction. **d**, Measured field map in the axial  $18 \times 20$  cm<sup>2</sup> planes for the constructed magnet distribution before shimming. The  $17 \times 14$  cm<sup>2</sup> ovals outline the approximate brain dimensions. **e**, CAD model of shim magnet distribution for fine tuning of the field. The smaller shim magnets' axial positions were fixed, but the size ( $< 1/4$ " cube) and the dipole direction were varied. **f**, Measured field map of the shimmed magnet, showing an improvement in the field linearity in  $x$ .

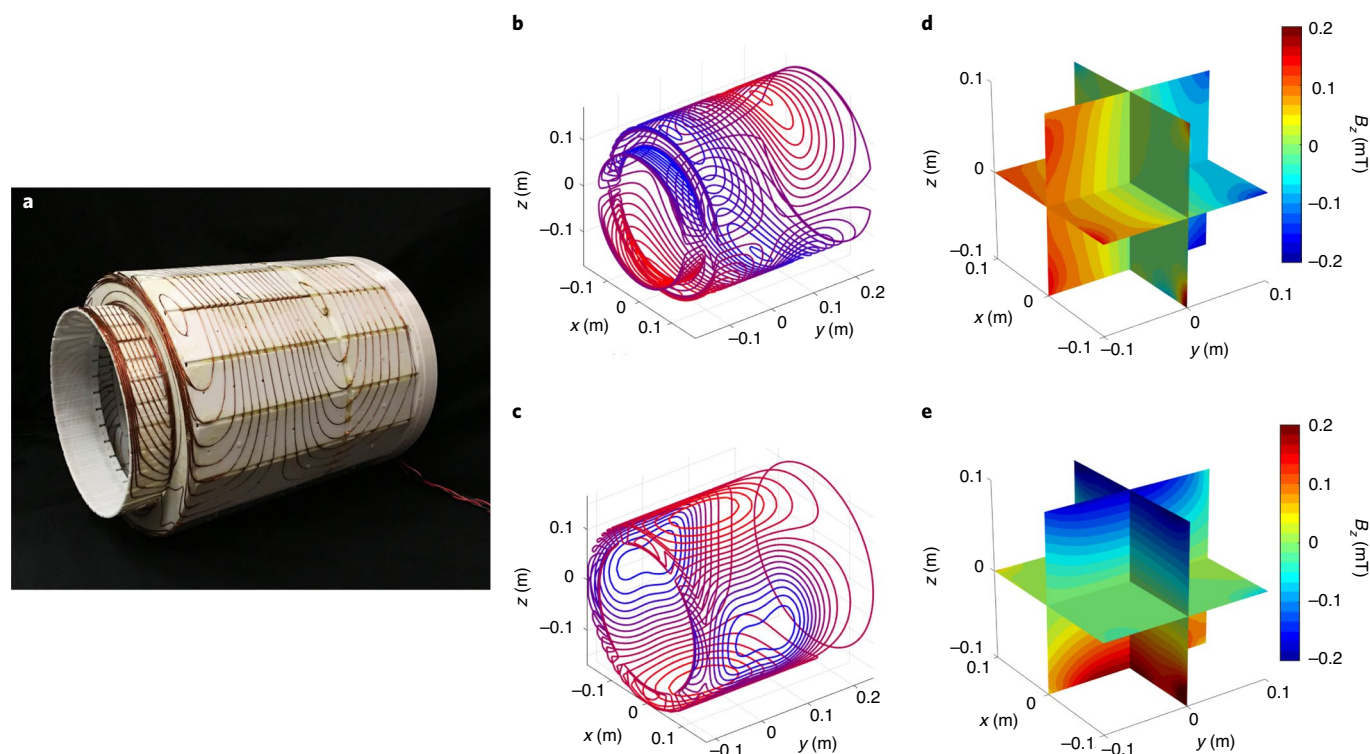
and variable resolution in the image. If relatively small, this distortion can be corrected using a model-based generalized image reconstruction technique<sup>30</sup> utilizing a priori knowledge of the fields. These generalized techniques employ a forward model of the time domain signal evolution in response to the known encoding non-linear fields<sup>19,28,29,31,32</sup>. Our encoding model uses the measured field maps of the built-in readout gradient (Fig. 2f) and gradient coils (Fig. 3c,e) and models the time domain-encoding process of our 3D RARE sequences.

We solve for the image using an iterative conjugate gradient algorithm implemented in MATLAB (MathWorks) with graphical processing units (GPUs). Supplementary Fig. 1 shows a T2-weighted 3D image of a roughly 11-cm-diameter grapefruit with no visible distortion. Figure 5 shows brain images of three healthy participants with an image resolution of approximately  $2.2 \times 1.3 \times 6.8$  mm<sup>3</sup>. This approximate resolution is calculated from a linear fit of the field maps, but the resolution actually varies slightly over the FOV due to the encoding field nonlinearities. The proof-of-principle images were acquired in an RF shielded room. The top three rows show proton density-, T1- and T2-weighted contrasts in the same participant (participant 1), followed by T2-weighted images in two additional participants (participants 2 and 3). The participant 3 FFT image (bottom row) was formed using a conventional reconstruction technique on the T2 data of participant 3, which assumed linear field gradients instead of the measured nonlinear fields. Comparing this with the generalized reconstruction technique demonstrates the distortion improvements achievable using a priori information of the encoding fields. However, some image distortion remains

towards the periphery where  $G_x$  is less linear. With the exception of T2-weighted images for participant 3, each image was acquired in  $\sim 10$  min. T2-weighted data for participant 3 were acquired in 19 min to allow for more averages and a higher SNR.

## Discussion

Our portable scanner is capable of generating standard brain MRI contrasts found on low-field clinical scanners (including T1-, T2-, inversion recovery-prepped T2-, proton density- and diffusion-weighted images) that are routinely used for detection, diagnosis and monitoring of clinically important brain pathology. The scanner offers superior soft tissue contrast resolution compared with other imaging modalities available for POC use, such as ultrasound, DXR and computed tomography, which are additionally limited by acoustic shadowing (ultrasound), beam hardening artefacts (DXR and computed tomography) from bone and calcified structures, ionizing radiation (DXR and computed tomography) and poor ability to distinguish certain central nervous system anatomic structures (for example, grey versus white matter, and subdural versus extradural spaces). Although both the spatial resolution and sensitivity of this scanner are less than that of a high-field MRI, the performance is sufficient to detect and characterize serious intracranial processes at the POC, such as haemorrhage, hydrocephalus, infarction and mass lesions. Indeed, our portable, compact, affordable device could extend the reach of MRI to answer critical, time-sensitive questions in settings where MRI is not currently available, including urgent care centres, emergency rooms, intensive care units, sports arenas, oncology clinics, remote field



**Fig. 3 | Gradient coil design.** **a**,  $G_y$  and  $G_z$  gradient coils with wires press-fit into a tiered cylinder 3D-printed former. The  $G_y$  gradient coil is on the outer surface and  $G_z$  gradient coil is on the inner surface. The tiered shape allows for maximum diameter (34.8 cm) and length (42.7 cm) within the magnet. **b,c**,  $G_y$  (**b**) and  $G_z$  (**c**) gradient coils' current density contours, designed with a stream function boundary element method optimized for linearity in the 20-cm ROI. **d,e**, Measured gradient coil field maps for 1 A of drive current in the  $G_y$  (**d**) and  $G_z$  coils (**e**). The  $G_y$  and  $G_z$  coil efficiencies were 0.6 and  $0.8 \text{ mT m}^{-1} \text{ A}^{-1}$ , respectively.

hospitals (for example, for military and humanitarian assistance missions) and perhaps even ambulances.

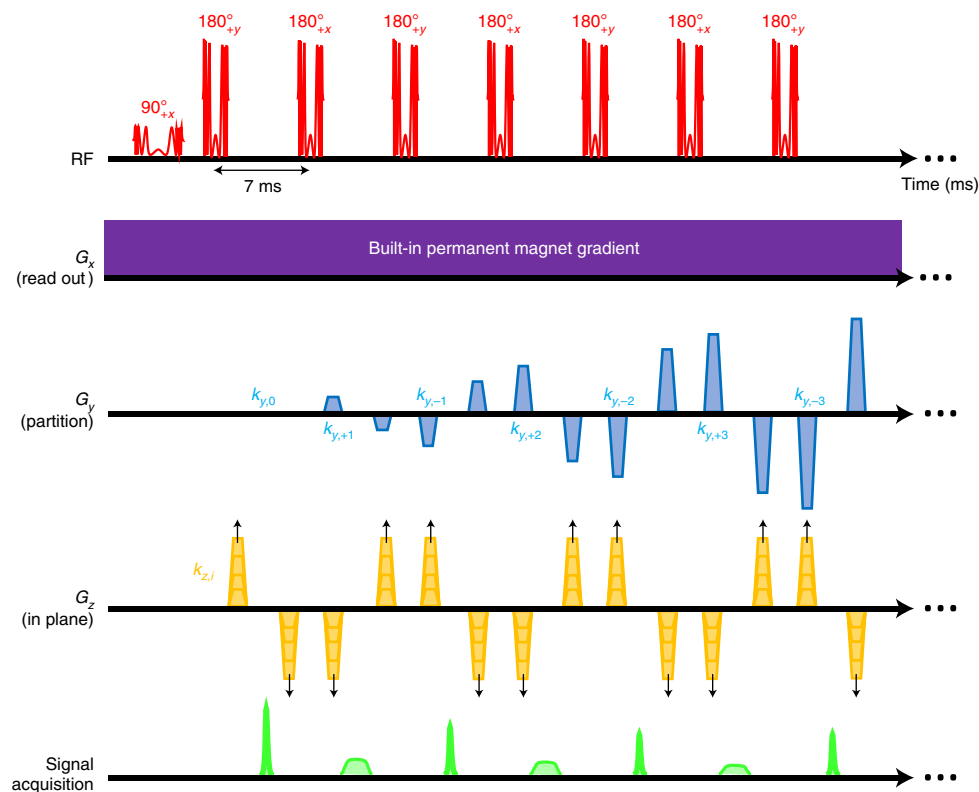
Although our proposed MRI scanner design fulfils many of the requirements for a POC brain-imaging device, several considerations require additional attention. The encoding field nonlinearities and their effect on the image are analysed in Fig. 6. The error maps show the percentage difference between the measured and ideal maps. The nonlinearity and resulting error are most severe in the permanent readout gradient,  $G_x$ , which has a 6.8% average error and 46.6% maximum error in the 17-cm circular ROI. This leads to a nonlinear mapping of voxels in the image that manifest as geometric distortion when the simple FFT reconstruction is used (represented by the spatial deformation maps in Fig. 6). The generalized reconstruction corrects for most of the spatial deformation, but instead, the variability in the local field gradient manifests as spatial varying image resolution. For example, the average  $G_x$  gradient is  $7.6 \text{ mT m}^{-1}$  with a  $2.2 \text{ mT m}^{-1}$  standard deviation in a  $17 \times 14 \text{ cm}^2$  ellipse ROI (approximate brain size). With our imaging parameters, this corresponds to an average resolution of 1.2 mm and a standard deviation in the local resolution of 0.45 mm. The nonlinearity is less severe for  $G_z$  and  $G_y$ , motivating the potential use of the FFT in those dimensions to decrease the computational burden of the generalized reconstruction.

Currently, image distortion is not fully addressed by our generalized reconstruction algorithm. Specifically, signal aliasing may be occurring due to the curvature of the field map isocontours, rendering the encoding fields non-orthogonal—a situation not included in the model. Remaining geometric distortions may also have contributions from measurement errors in the encoding field maps. These distortions become more marked further from isocentre, where the nonlinearities are more severe (Fig. 6).

The high temperature coefficient of magnetic remanence (around  $-0.1\% \text{ } ^\circ\text{C}^{-1}$ ) and coercivity (around  $-0.5\% \text{ } ^\circ\text{C}^{-1}$ ) in NdFeB material (<http://www.advancedmagnets.com/custom-magnets/>) results in variation in the  $B_0$  field with room temperature, and could contribute to errors in the reconstruction model. Before each dataset is acquired, the centre Larmor frequency is set, reducing large off-resonance effects from temperature drift. Furthermore, a global  $B_0$  offset variable is adjusted in the reconstruction model to account for differences in the experimental  $B_0$  field compared with the previously measured  $B_0$  field maps. However, we currently assume that there are no significant temperature changes on the time scale of each image acquisition ( $\sim 10$  min). To improve the accuracy of the reconstruction model, field probes can be used to track global<sup>19</sup> or local changes in the  $B_0$  field during data acquisition.

The power budget of the scanner is an important consideration for portability and POC use. Typical 1.5-T commercial superconducting scanners consume  $10\text{--}30 \text{ kWh}^{-1}$  per examination<sup>33</sup>. The cryocooler system alone requires 6–8 kW of power. The metallic cryostat also necessitates shielded gradient coils, which are  $\sim 30\%$  less efficient. The GPAs needed to drive these large shielded gradient coils are a significant source of power consumption. Ramping down a standard scanner to operate at low field (for example,  $0.55 \text{ T}$ )<sup>8</sup> does not reduce the total power consumption significantly. However, compact POC scanner designs can yield substantial reductions in power consumption. For example, the Hyperfine 64-mT scanner (<https://www.hyperfine.io/portable-mri>) operates with a maximum power consumption of 1,650 W for the entire system, including the console, RF power amplifier and three axes of gradient amplifiers.

Our presently described system reduces power requirements with a compact design and the use of permanent magnets for both the  $B_0$  field and readout gradient field. The elimination of the



**Fig. 4 | MRI pulse sequence diagram.** The 3D RARE pulse sequence is shown for the proton density-weighted sequence. The RF applies the  $90^\circ$  excitation chirped pulse (3.2 ms; 100 kHz sweep) followed by a train of  $180^\circ$  chirped refocusing pulses (1.6 ms; 100 kHz sweep). The phase of the pulses follows a phase cycling scheme that prevents mixing of the resulting FID and spectral echoes. The  $G_x$  readout gradient is the built-in permanent magnet encoding field, and therefore is continuously applied throughout the acquisition. The  $G_y$  gradient produces phase-encoding blips that vary along the echo train for partitioning data in the y dimension, completing the 23 encodes in each shot. The  $G_z$  phase-encoding blips are incremented shot to shot, requiring 97 repetition time periods to complete the encoding. The signal acquisition alternates between the narrow FID echoes and wider spectral echoes. The sequence is converted to T1 weighting with the addition of an initial inversion pulse. In the T2-weighted sequence, the ordering of the  $G_y$  phase-encoding blips is re-arranged so that the centre of k-space is captured at  $TE_{eff} = 167$  ms.

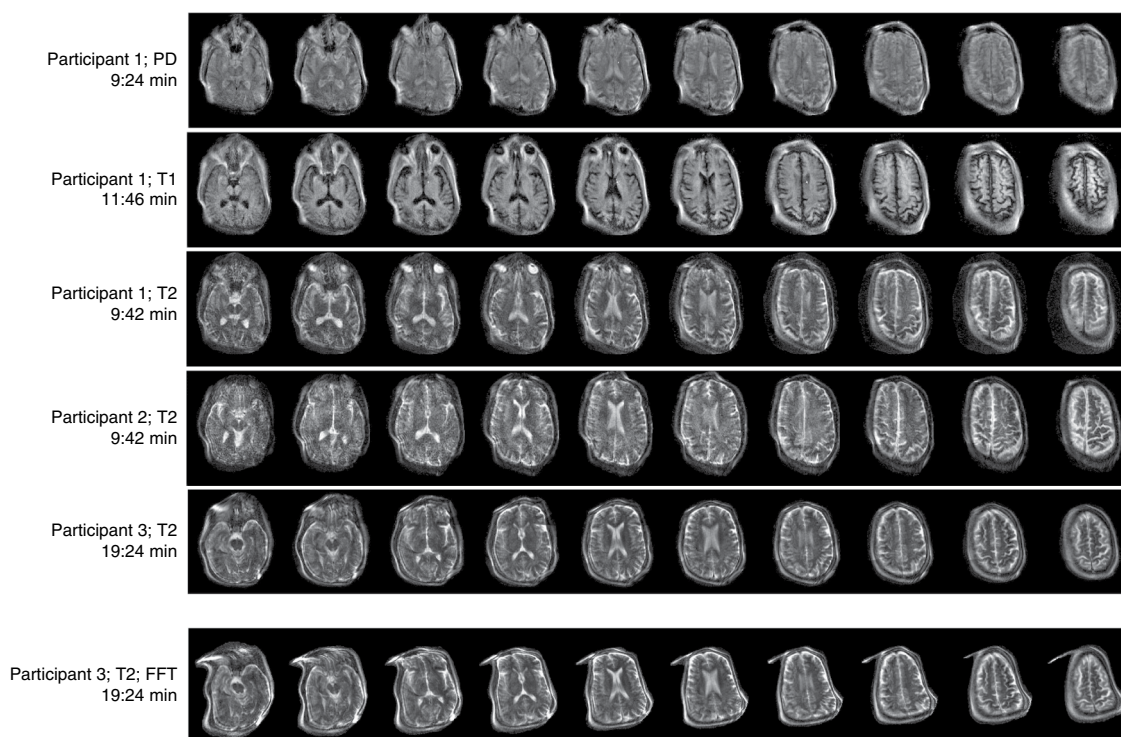
superconducting system reduces the power consumption significantly. Additionally, only two switchable GPAs are needed to drive the small, unshielded phase-encoding gradient coils, which typically operate at a lower amplitude and duty cycle than readout gradients. This further reduces the power budget compared with the three GPA implementations found in standard MRI scanners. The sub-systems of the scanner currently consume a total of  $\sim 800$  W and can all be operated from a standard power outlet. This includes  $\sim 400$  W for the RF transmit, 50 W for the gradient amplifiers (10 A into  $2\Omega$  for each coil at a 5% duty cycle and 40% efficiency), 200 W for the console electronics and 75 W for the computer. The previously introduced rotating permanent magnet + RF encoding approach<sup>22</sup> is expected to require slightly more power, requiring a stepper motor and additional RF power but omitting both gradient channels.

Future iterations of the scanner design could focus more on industrial patient interfacing and workflow considerations. The compact size of the scanner results in a tight fit around the head, requiring special attention to the mechanical design of this area, including entrance and exit patient positioning (especially for intubated and highly monitored patients) and airflow and monitoring within the bore. However, the volunteers imaged with the scanner found it to be comfortable during their  $>45$ -min acquisition session. Moreover, our head-only magnet design improves patient comfort by eliminating confinement around the body. Furthermore, our design allows acoustically quiet operation, eliminating the need for ear plugs.

The preliminary images presented here were acquired in an electromagnetically shielded room, such as that of traditional scanners. This RF shielded scanner suite eliminates electromagnetic interference (EMI), which can otherwise degrade image quality (SNR) and can introduce artefacts. In our portable system, although a copper shield was placed between the gradient coils and RF head coil, this was insufficient to fully eliminate EMI in human imaging. The openings in these shields are small compared with the relevant wavelength of the system's MRI signal (89 m), and the built-in shield was shown to be sufficient to prevent EMI when imaging small phantoms or fruit (Fig. 5). However, when imaging humans, the body parts outside the shield act as an antenna, which conducts EMI into the MRI receiver coil. Therefore, for our pilot human imaging validation, we operated the scanner inside a traditional Faraday cage to eliminate this source of image degradation. Work is ongoing to actively record and remove interference using external pick-up coils that can monitor environmental EMI during imaging<sup>34,35</sup>.

To maximize image SNR, a limited bandwidth RF receive coil was chosen. This incurs some image shading in the readout direction that is partially offset by the increased coil sensitivity at the FOV edge (near the wires). Ongoing efforts include optimizing RF coil designs to increase the SNR and extend the FOV to more inferior brain regions, as well as testing and validation with specific brain pathologies, such as small-vessel white matter disease, in addition to testing healthy participants. Preliminary work also suggests that diffusion-weighted imaging, which is critical to certain





**Fig. 5 | 3D T2-, T1- and proton density-weighted images of the brain in healthy adult volunteers.** A subset of the acquired 23 partitions are shown. Image resolution =  $-2.2 \times 1.3 \times 6.8 \text{ mm}^3$ . The first five rows show images reconstructed with the generalized forward model-based reconstruction method. Row 1 (participant 1; male; 63 years old): proton density (PD) images acquired with 3D RARE (repetition time/ $TE_{\text{eff}}$  = 2,900 ms/14 ms; acquisition time = 9:24 min; two averages). Row 2 (participant 1): T1-weighted images acquired with inversion-prepped 3D RARE (inversion time/repetition time/ $TE_{\text{eff}}$  = 400 ms/1,830 ms/14 ms; acquisition time = 11:46 min; four averages). Row 3 (participant 1): T2-weighted images acquired with the 3D RARE sequence (repetition time/ $TE_{\text{eff}}$  = 3,000 ms/167 ms; acquisition time = 9:42 min; two averages). Row 4 (participant 2; male; 63 years old): T2-weighted images acquired with the 3D RARE sequence (repetition time/ $TE_{\text{eff}}$  = 3,000 ms/167 ms; acquisition time = 9:42 min; two averages). Row 5 (participant 3; female; 53 years old): T2-weighted images acquired with the 3D RARE sequence (repetition time/ $TE_{\text{eff}}$  = 3,000 ms/167 ms; acquisition time = 19:24 min; four averages). Row 6 (participant 3; FFT): T2 data reconstructed with a conventional FFT reconstruction instead of the generalized method. This last image demonstrates the geometric distortion that results from the nonlinear encoding fields when the field maps are not included in the reconstruction model. The measured SNRs in the images were 127, 80, 68, 65 and 124 for the image acquisitions shown in rows 1–5, respectively.

applications, such as acute stroke detection, is also possible with our unconventional scanner architecture<sup>36</sup>.

## Outlook

This scanner design could serve as a foundation to develop and clinically validate portable MRI devices for affordable, POC detection, assessment and monitoring of diverse medical applications in addition to the diagnostic whole-brain imaging applications discussed (for example, our architecture could be minimally modified for extremity and neonatal imaging). Moreover, extending the general concept of liberating the MRI design from traditional constraints might lead to even more exotic designs with extreme portability, such as hand-held devices. Devices that generate limited FOV images or profiles directly under a single-sided scanner (<https://promaxo.com/> and ref. <sup>27</sup>) could be used for diverse real-time emergency and urgent care indications, such as the detection, delineation and serial monitoring of soft tissue pathologies (for example, pleural effusions, extremity abscesses requiring drainage or subdural/epidural haematomas), or to provide guidance for interventional procedures (for example, catheter placement, lumbar punctures<sup>37</sup> or biopsies; <https://promaxo.com/>). Such devices have the potential to complement or replace the roles of other (often suboptimal or more limited) portable imaging modalities.

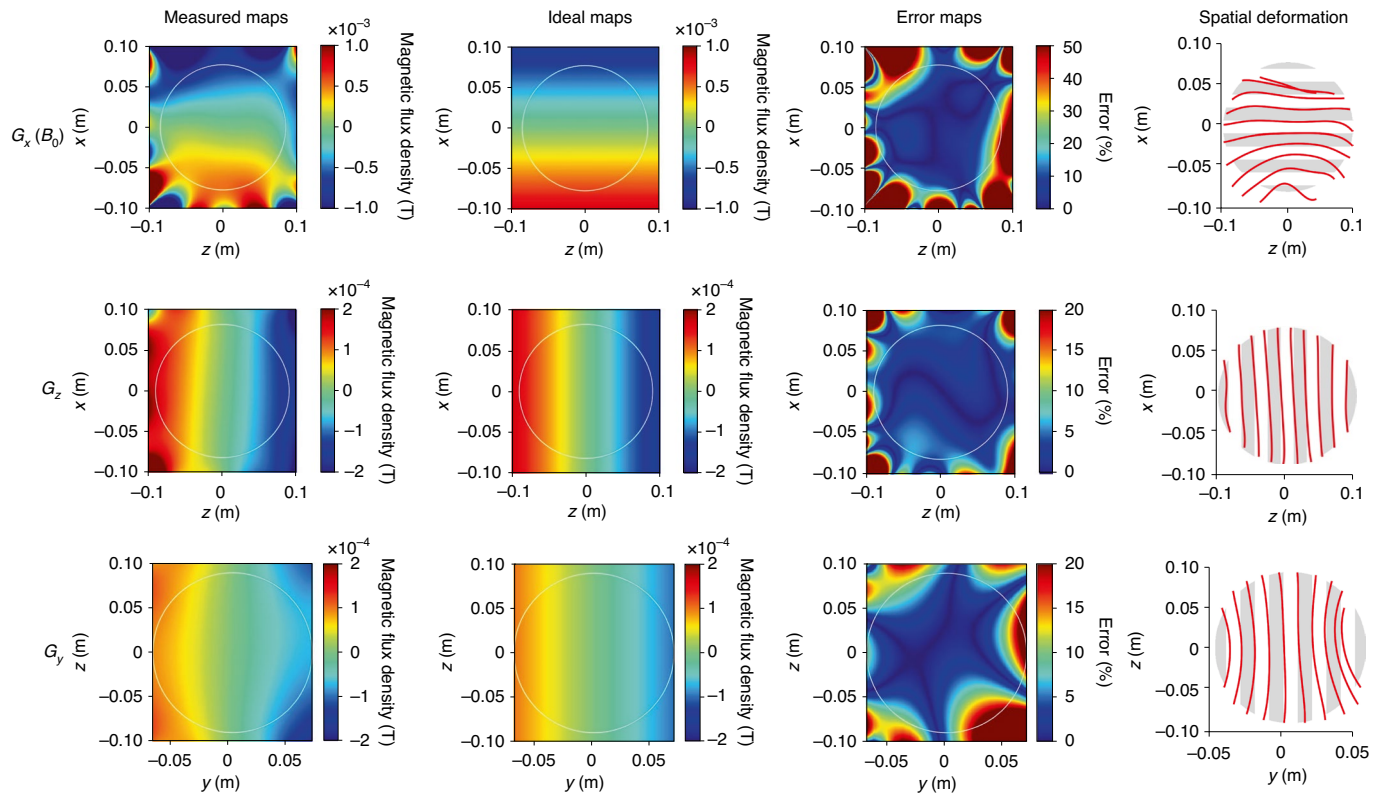
In summary, we have introduced an MRI scanner architecture based on a compact, lightweight, low-field, permanent magnet array, with built-in field variation for MRI readout encoding and

efficient electromagnetic gradient coils for phase encoding. Our design leverages advanced image reconstruction methods to correct for magnetic field imperfections, freeing the hardware from traditional constraints. Unlike conventional MRI scanner designs, this approach could allow for POC operation due to the magnet's modest size, the lack of cryogenics and the intrinsic safety of the low-field, magnetically self-shielded Halbach configuration. Both mobility and POC potential are also facilitated by the low power consumption and low acoustic noise afforded by our built-in readout gradient. The presented in vivo brain images show the potential of the scanner for clinical application at the POC, which could expand the access of MRI to patient populations now underserved by traditional MRI limitations.

## Methods

**Permanent magnet construction.** The head-sized permanent magnet was designed using a genetic optimization framework previously described by Cooley et al.<sup>14</sup>. The dimensions and basic geometry of the sparse Halbach magnet were determined based on human anatomy and trade-offs between field strength and size. The ROI is defined as a 20-cm sphere with the isocentre at 17.8 cm from the inferior end of the magnet (constrained by the shoulders). The magnet is asymmetric, extending 27.9 cm above the isocentre (in the superior direction) to improve homogeneity. A booster ring of magnets is added near the shoulders to compensate for the field fall-off effects there.

The Halbach cylinder is made up of square cross-section permanent magnet rungs divided into two full layers at diameters of 41 and 50 cm. Each layer contains 24 rungs that are 45.7 cm in length. The additional Halbach booster ring near the patient's shoulders has a diameter of 32 cm and a length of 2.54 cm (one magnet



**Fig. 6 | Analysis of the measured encoding field maps ( $G_x$ ,  $G_z$  and  $G_y$ ) in the central field map slices.** The ideal maps are calculated as a linear fit to the measured maps. The error maps show the percentage difference between the measured maps and ideal maps. The colour range is higher (up to 50%) for the  $G_x$  gradient. Spatial deformation maps show the resulting image distortion that occurs when the ideal linear map is assumed (instead of the measured map). The nonlinearities and spatial deformation are most severe in the  $G_x$  encoding map, which is generated by the built-in permanent magnet gradient. The  $G_x$  analysis shows high errors near the periphery and severe spatial deformation approaching signal singularities in some locations. In contrast, the gradient coil map ( $G_z$  and  $G_y$ ) errors and spatial deformation maps are more benign.

row). NdFeB rare-earth magnetic material was chosen because of its high remnant flux density, coercivity and lower cost compared with SmCo. The magnet was constructed with stock 1'' NdFeB cubes (NB040 and NB041; Applied Magnets). The use of standardized 1'' NdFeB cubes eases the cost and construction of the magnet, and the sparsity of the design reduces the cost and weight (albeit at the cost of field strength).

In the full magnet geometry, there are 888 predetermined potential locations for the NdFeB cubes. A genetic algorithm determined the placement of either N42 and N52 grade NdFeB cubes or plastic spacers at each location. The optimization was constrained to produce a mean  $B_0$  of  $>70$  mT with a monotonic encoding field and reasonable total field range<sup>14</sup>. The resulting design, shown in Fig. 2, contains 342 and 299 N42 and N52 NdFeB cubes, respectively (~80 kg of NdFeB material).

The non-magnetic housing for the NdFeB material uses 1'' cross-section structural fibreglass square tubes that contain the magnet material. The rungs are mechanically supported by seven 1.27-cm-thick acrylonitrile butadiene styrene plastic rings with waterjet-cut square holes rotated in the Halbach configuration. The design also contains 48 octagonal holes meant to hold trays of smaller shim magnets. Threaded brass fastening rods and fibreglass dowel spacers increase the structural integrity. After full assembly of the mechanical housing, a pushing jig is used to populate the NdFeB cubes into the corresponding rungs. The cube magnets repel each other within the rungs, so the jig is needed to temporarily extend the fibreglass rung length so the magnets can float apart. Then, the jig is used to push all of the magnets into contact within the housing and bolt an end cap on the tube. This is repeated for all 48 rungs. The NdFeB material is handled with caution as serious injury could result from the forces between the NdFeB cubes. The resulting magnet structure has a length of 49 cm, an outer diameter of 57 cm, an inner diameter of 35 cm, a bore access diameter of 27 cm and a weight of 122 kg.

A field-mapping robot was constructed to measure the field pattern in the permanent magnet and gradient coils. The robot was based on a modified build-your-own computer numerical control (CNC) router kit (Avid CNC), which rastered a three-axis gaussmeter probe (THM1176; Metrolab Technology). MATLAB software was used to simultaneously control the stepper motors to traverse the probe through the magnet's ROI and record the gaussmeter field measurements.

The field at construction was dominated by a first-order field variation, but the existing nonlinearities caused severe image distortion and some singularities (aliasing). Therefore, a target-field shimming iteration was used to refine the built-in encoding field of the magnet<sup>23</sup>. This was achieved with an optimized population of the 48 shim trays (each containing 42 shim magnet locations, for NdFeB cubes of up to 6.35 mm). The orientation (dipole direction) and size of NdFeB shim magnets at each of the 2,016 potential shim locations was optimized to minimize the RMSE deviation from an ideal linear target gradient in the ROI. This calculation used an interior-point MATLAB optimization with each shim magnet modelled as an ideal magnetic dipole. The varying size of the resulting dipoles was practically realized by gluing smaller magnet pieces together. The resulting shape and orientation of each shim magnet were designed into the 3D-printed shim trays.

**Gradient coil construction.** The gradient coils were designed to create linear target-field gradients in the  $y$  and  $z$  directions in the imaging ROI<sup>23,38</sup>. The mechanical surfaces of the two coils were predetermined to be on the inner and outer surfaces of a tiered cylinder former designed to fit snugly inside the magnet (length = 42.7 cm; diameter 1 = 34.8 cm; diameter 2 = 26.4 cm). The current stream functions of the coils were optimized on a 20-cm-diameter ROI using a stream function boundary element method solver based on a published toolbox<sup>39</sup>. The achievable current density at the truncated end of the coil (the shoulder side) is limited by the practical density of the windings in this area, which proved to be the main constraint limiting the coil's efficiency and linearity. Based on the optimized current stream function, the coil winding patterns were designed for a target gradient efficiency of  $0.7 \text{ mT m}^{-1} \text{ A}^{-1}$  and a resistance of  $<2 \Omega$ . American wire gauge 18 wire was press-fit into wire winding pattern grooves in a 3D-printed former. The field-mapping robot was used to measure the field pattern when each coil was driven with 1 A inside the magnet. The resulting gradient efficiencies, inductances and resistances were determined to be  $0.575$  and  $0.815 \text{ mT m}^{-1} \text{ A}^{-1}$ ,  $514$  and  $336 \mu\text{H}$ , and  $1.9$  and  $1.2 \Omega$  for  $G_y$  and  $G_z$ , respectively. For the imaging sequences described here, less than 10 A peak current was used at a low-duty cycle (3–5%) allowing for passive air cooling. The low power requirements of the gradient systems will allow for the future integration of very low-cost, low-power, small-footprint operational amplifier-based drivers<sup>40</sup>.



**RF coil construction.** The RF coil (Fig. 1b,c) is based on a compact spiral helmet design<sup>41</sup> used for transmit and receive with a passive transmit–receive switch. The coil is wound on a tightly fitting helmet former of the following inner dimensions: 21 cm (anterior–posterior); and 17 cm (medial–lateral)<sup>41</sup>. The windings extend 10.7 cm from the top of the head. The close-fitting spiral pattern provides favourable RF receive efficiency and sensitivity. However, when the windings are uniformly distributed on the helmet, the resulting  $B_1$  field is inhomogeneous, with an 87% higher field produced at the top of the head compared with the bottom in simulation. When used as a transmit–receive coil, the inhomogeneous nature of the resulting  $B_1+$  pattern causes variable flip angles in the brain and image artefacts. To improve the  $B_1+$  homogeneity, the winding distribution was empirically adjusted using Biot–Savart simulations, resulting in a total of 12 asymmetric windings with a higher turn density near the bottom of the coil. This reduced the  $B_1$  range in the helmet by 79% compared with the uniform winding design. The coil was constructed on a 3D-printed polycarbonate former with winding grooves. The non-uniform turn distribution was wound with Litz wire (American wire gauge 20; 5/39/42; New England Wire) and tuned and matched to 50  $\Omega$  at the system's 3.39 MHz Larmor frequency with non-magnetic capacitors. The loaded and unloaded quality factors ( $Q$ ) of the coil were 150 and 225, its inductance was 69  $\mu$ H and its simulated efficiency was 28  $\mu$ T A<sup>-1</sup> (Supplementary Fig. 1). A rectangular excitation was observed to achieve a 90° flip angle (over a limited bandwidth) with a power and pulse width of 44 W and 80  $\mu$ s, respectively.

**Other hardware.** A passive crossed diode-based, lumped element quarter-wave 50- $\Omega$  transmit–receive switch is used with the RF coil. Reception uses a low-noise 50- $\Omega$  input impedance, a 37-dB gain pre-amplifier (MITEQ; model AU-1583) and a 24-dB second-stage amplifier (Minicircuits; model ZFL-500LN+). Additional hardware includes: a Tecmag Bluestone MRI console, AE Techron 7224 gradient amplifiers, a 2-kW peak-power RF power amplifier (Tomco Technologies; model BT02000-AlphaS-3MHz) and a patient table constructed from T-slot aluminium extrusions. While this equipment is well suited for prototyping and validating the scanner design, the console, gradient amplifiers, RF amplifier and patient table could be replaced with custom designs that prioritize cost and weight<sup>40,42,43</sup>.

**Acquisition method.** The permanent magnet readout encoding field is always on, causing an inhomogeneous  $B_0$  field ( $\Delta B_0/B_0 \approx \sim 2\%$ ) and a wide Larmor frequency bandwidth in the ROI ( $\sim 80$  kHz). For wide-bandwidth RF excitation and refocusing in the spin-echo train, shaped frequency-swept RF pulses (wideband, uniform rate, smooth truncation (WURST) pulses) were transmitted instead of rectangular single-frequency pulses (hard pulses). This use of WURST pulses for MRI in an inhomogeneous field has been described previously<sup>21,24</sup>. Although similar to a rectangular chirped pulse, WURST pulses have a soft taper on the rising and falling edge of the pulse to reduce ringing artefacts and achieve a smooth transition at the edges of the frequency band of excited spins. The excitation and refocusing pulses used in our sequences are 3.2 and 1.6 ms long (respectively) with a 100-kHz linear frequency sweep and a WURST-40 amplitude envelope. The simulations in Supplementary Fig. 2 demonstrate the bandwidth coverage of the pulses and the robustness to  $B_1$  variation in the refocusing pulses.

The linear frequency sweep of the RF pulses imparts an undesired quadratic phase on the spins across frequency. When the background field gradient is held constant during excitation and refocusing, the quadratic phase can be removed from odd-numbered echoes by setting the frequency sweep rate of the refocusing pulse to be twice as fast as that of the excitation pulse<sup>44</sup>. The resulting quadratic phase cancellation in the odd echoes of the RARE echo train results in free induction decay (FID) echoes (classic spin echoes). However, the even-numbered echoes contain the quadratic phase, resulting in spectral echoes in which different spin isochromats refocus at different time points. Confounding mixing of the FID and spectral echoes can result from flip angle errors. To alleviate this, phase cycling of the RF pulses (alternating between 0 and 90°) is used to form two spin coherence pathways<sup>23</sup>. Although there are schemes to combine data from the two types of echo<sup>21,24</sup>, we reconstruct only the spectral echoes to limit data inconsistency.

We use 3D RARE sequences, which support standard T2, inversion recovery-prepped T2, T1, proton density and diffusion contrasts. Sequences were implemented in TNMR version 3.4.31 for use with the Tecmag console. Since no slice-selective gradient is employed, the system acquires 3D encoded axial imaging where the  $y$  phase-encode gradient is used for partitioning the 3D data into  $\sim 7$ -mm-thick image partitions. Figure 4 depicts the basic pulse sequence diagram, including the chirped RF pulses, the  $G_x$  phase-encoding blips (varying down the spin-echo train), the  $G_z$  phase-encoding blips (incrementing shot to shot for each spin-echo train) and the  $G_y$  permanent magnet readout gradient (always on). The resulting spin echoes (signal acquisition line) show the previously described alternating FID-echo and spectral-echo behaviour<sup>24</sup>.

For T2 weighting, the  $y$  dimension (partition) phase encoding is performed along the echo train with a  $k$ -space trajectory placing the centre of  $k$ -space in the middle echo. The  $z$ -dimension gradient phase encoding is incremented shot to shot. The proton density sequence uses a centre-out  $k$ -space ordering down the echo train. The T1 sequence is similar but includes an inversion recovery preparation pulse.

Diffusion weighting in the RARE sequences is expected to be small. The diffusion weighting ( $b$  value) from a static gradient in a RARE sequence is given by  $b = 1/12\gamma^2 G^2 \tau^3$  where  $\gamma$  is the proton gyromagnetic ratio,  $G$  is the fixed gradient amplitude and  $\tau$  is the RARE echo spacing<sup>45</sup>. For the 7-ms echo spacing used and the  $G = 7$  mT m<sup>-1</sup> fixed gradient, diffusion weighting is minimal with an expected  $b$  value of  $< 1$  mm<sup>-2</sup>. Future plans for diffusion-weighted neuroimaging will require the addition of a diffusion-encoding module between the RF excitation pulse and the first echo<sup>36</sup>.

**In vivo experiments.** Participants were setup in a supine position on the detachable patient table for imaging. Before attaching the patient table to the scanner, the RF coil was positioned on the participant. A 1-min, low-resolution image acquisition was used to confirm the proper positioning of the participant's head in the coil and magnet. All in vivo images were acquired with a matrix size of 256  $\times$  97  $\times$  23 and an approximate resolution of 2.2  $\times$  1.3  $\times$  6.8 mm<sup>3</sup>. Participant 1 was imaged with the 3D RARE proton density-weighted sequence (repetition time/effective echo time (TE<sub>eff</sub>) = 2,900 ms/14 ms; two averages; acquisition time = 9:24 min), the inversion-prepped 3D RARE T1-weighted sequence (inversion time/repetition time/TE<sub>eff</sub> = 400 ms/1,830 ms/14 ms; four averages; acquisition time = 11:46 min) and the 3D RARE T2-weighted sequence (repetition time/TE<sub>eff</sub> = 3,000 ms/167 ms; two averages; acquisition time = 9:42 min). Participant 2 was imaged with the 3D RARE T2-weighted sequence (repetition time/TE<sub>eff</sub> = 3,000 ms/167 ms; two averages; acquisition time = 9:42 min). Participant 3 was imaged with the 3D RARE T2-weighted sequence (repetition time/TE<sub>eff</sub> = 3,000 ms/167 ms; four averages; acquisition time = 19:24 min). The study was approved by the institutional review board of Partners HealthCare and written informed consent was obtained before scanning.

**Image reconstruction method.** The images are reconstructed from the data using a generalized encoding matrix model (to describe the expected signal based on the measured field maps) and an iterative linear solver (to determine the image)<sup>19,28,29,31,32</sup>. This provides a more accurate relationship between the encoded signal and the object than the Fourier model (which assumes linear encoding fields) and, in principle, alleviates image distortion from the imperfect encoding fields.

A full 3D reconstruction can be done using all three encoding field maps, but to reduce the matrix size the data are partitioned in the  $y$  direction using the FFT. The generalized reconstruction method is then used to reconstruct each 2D axial image. Specifically, the encoding matrix represents the phase at each time domain sample point in an echo, imparted by the  $G_x$  readout encoding field and the  $G_z$  phase-encoding blips. Without relaxation effects, the assumed signal equation for the readout time point,  $t$ , and the  $n$ th  $G_z$  phase encode is modelled as:

$$s_n(t) = \sum_r e^{-2\pi r(G_x(r) + I(n)G_z(r)\tau)} m(r)$$

where  $r$  is the 2D position,  $\gamma$  is the gyromagnetic ratio in Hz/Tesla,  $G_x$  is the nonlinear built-in readout gradient field map (in units of Tesla),  $I(n)$  is the  $G_z$  scaling factor for the  $n$ th phase-encode blip,  $G_z$  is the 2D phase-encoding gradient field map,  $\tau$  is the length of the phase-encode blip and  $m$  is the image. A coil sensitivity weighting is not included because we assume a uniform receive sensitivity from the volume coil.

This equation can be simplified as a matrix-vector product, where the matrix contains the known field quantities ( $G_x$  and  $G_z$ ) and the vector is the list of image pixels to be estimated. Therefore, image reconstruction is a linear inverse problem that we solve using the conjugate gradient method. The system matrix is very large in our case; therefore, we do not store in memory and instead compute its rows online, which is very fast. The  $G_x$  and  $G_z$  field maps contain a few million elements each, and therefore fit easily in the global shared memory of modern GPUs such as the Tesla K20c (5 GB) or the more recent Tesla P100 (16 GB). Implementation of the matrix-vector product ( $Ax$  and  $A^Hx$ , where  $^H$  is the complex-transpose operation) takes a couple of seconds in the GPU compared with  $\sim 1$  h on a single central processing unit. To minimize the total computation time, we also employ a preconditioner, which is the diagonal matrix comprised of the square of the diagonal entries of the system matrix correlation matrix ( $C = A^H A$ ). This is a good preconditioner for this problem since it is: (1) ultra-rapid to compute; (2) trivial to invert; and (3) reduces the condition number of the problem from  $\sim 133$  to  $\sim 2$ . As a result, iterative reconstruction of an image with a matrix size of 220  $\times$  180 (FOV = 22  $\times$  18 cm<sup>2</sup>) requires five to ten iterations at the 0.1% convergence level, which represents a total time of  $< 20$  s.

We apply an intensity correction to the images to alleviate shading caused by  $B_1$  inhomogeneity. This is done by masking each 2D image and dividing it by a low-pass-filtered version of itself. Image SNR calculations were performed on the FFT reconstructed version of the image, to reduce the confounding effects of noise amplification in iterative reconstruction. The calculation was performed in a central partition magnitude image. SNR was calculated as the mean of a high-intensity ROI ( $\sim 30$  voxels) divided by the standard deviation of background ROI ( $\sim 800$  voxels). A factor of  $\sqrt{\pi/2}$  was applied to account for the Rician distribution of the magnitude image noise.

**Reporting Summary.** Further information on research design is available in the Nature Research Reporting Summary linked to this article.

### Data availability

The main data supporting the results of this study are available within the paper and its Supplementary Information. All reconstructed MATLAB image files and one exemplary raw dataset are available from GitHub at <https://github.com/czcooley/portable-MRI>.

### Code availability

The MRI data were analysed using custom code in MATLAB 2018b. Image reconstruction and processing code is available from GitHub at <https://github.com/czcooley/portable-MRI>. Field-mapping MATLAB code and TNMR files are available from the corresponding author upon request.

Received: 21 February 2020; Accepted: 3 October 2020;

Published online: 23 November 2020

### References

- GBD 2016 Neurology Collaborators. Global, regional, and national burden of neurological disorders, 1990–2016: a systematic analysis for the Global Burden of Disease Study 2016. *Lancet Neurol.* **18**, 459–480 (2019).
- Sánchez, Y. et al. Magnetic resonance imaging utilization in an emergency department observation unit. *West J. Emerg. Med.* **18**, 780–784 (2017).
- Beckmann, U., Gillies, D. M., Berenholtz, S. M., Wu, A. W. & Pronovost, P. Incidents relating to the intra-hospital transfer of critically ill patients. *Intensive Care Med.* **30**, 1579–1585 (2004).
- Mathur, A. M., Neil, J. J., McKinstry, R. C. & Inder, T. E. Transport, monitoring, and successful brain MR imaging in unsedated neonates. *Pediatr. Radiol.* **38**, 260–264 (2008).
- Warf, B. C. & East African Neurosurgical Research Collaboration. Pediatric hydrocephalus in East Africa: prevalence, causes, treatments, and strategies for the future. *World Neurosurg.* **73**, 296–300 (2010).
- Wald, L. L., McDaniel, P. C., Witzel, T., Stockmann, J. P. & Cooley, C. Z. Low-cost and portable MRI. *J. Magn. Reson. Imaging* **52**, 686–696 (2020).
- Geethanath, S. & Vaughan, J. T. Accessible magnetic resonance imaging: a review. *J. Magn. Reson. Imaging* **49**, e65–e77 (2019).
- Campbell-Washburn, A. E. et al. Opportunities in interventional and diagnostic imaging by using high-performance low-field-strength MRI. *Radiology* **293**, 384–393 (2019).
- Foo, T. K. F. et al. Lightweight, compact, and high-performance 3T MR system for imaging the brain and extremities. *Magn. Reson. Med.* **80**, 2232–2245 (2018).
- Matter, N. I. et al. Three-dimensional prepolarized magnetic resonance imaging using rapid acquisition with relaxation enhancement. *Magn. Reson. Med.* **56**, 1085–1095 (2006).
- Espy, M. A. et al. Progress toward a deployable SQUID-based ultra-low field MRI system for anatomical imaging. *IEEE Trans. Appl. Supercond.* **25**, 1–5 (2015).
- Sarracanie, M. et al. Low-cost high-performance MRI. *Sci. Rep.* **5**, 15177 (2015).
- Vaughan, J. T. et al. Progress toward a portable MRI system for human brain imaging. *Proc. Intl Soc. Mag. Reson. Med.* **24**, 0498 (2016).
- Cooley, C. Z. et al. Design of sparse Halbach magnet arrays for portable MRI using a genetic algorithm. *IEEE Trans. Magn.* **54**, 1–12 (2018).
- O'Reilly, T., Teeuwisse, W., Winter, L. & Webb, A. G. The design of a homogenous large-bore Halbach array for low field MRI. *Proc. Intl Soc. Mag. Reson. Med.* **27**, 0272 (2019).
- Ren, Z. H., Mu, W. C. & Huang, S. Y. Design and optimization of a ring-pair permanent magnet array for head imaging in a low-field portable MRI system. *IEEE Trans. Magn.* **55**, 1–8 (2019).
- Sarty, G. E. & Vidarsson, L. Magnetic resonance imaging with RF encoding on curved natural slices. *Magn. Reson. Imaging* **46**, 47–55 (2018).
- Moore, G. E. Cramming more components onto integrated circuits, reprinted from *Electronics*, volume 38, number 8, April 19, 1965, pp.114 ff. *IEEE Solid-State Circuits Soc. Newsl.* **11**, 33–35 (2006).
- Cooley, C. Z. et al. Two-dimensional imaging in a lightweight portable MRI scanner without gradient coils. *Magn. Reson. Med.* **73**, 872–883 (2015).
- Halbach, K. Design of permanent multipole magnets with oriented rare earth cobalt material. *Nucl. Instrum. Methods* **169**, 1–10 (1980).
- Stockmann, J. P., Cooley, C. Z., Guerin, B., Rosen, M. S. & Wald, L. L. Transmit array spatial encoding (TRASE) using broadband WURST pulses for RF spatial encoding in inhomogeneous  $B_0$  fields. *J. Magn. Reson.* **268**, 36–48 (2016).
- Cooley, C. Z., Stockmann, J. P., Sarracanie, M., Rosen, M. S. & Wald, L. L. 3D imaging in a portable MRI scanner using rotating spatial encoding magnetic fields and transmit array spatial encoding (TRASE). *Proc. Intl Soc. Mag. Reson. Med.* **23**, 0703 (2015).
- McDaniel, P., Cooley, C. Z., Stockmann, J. P. & Wald, L. L. A target-field shimming approach for improving the encoding performance of a lightweight Halbach magnet for portable brain MRI. *Proc. Intl Soc. Mag. Reson. Med.* **27**, 0215 (2019).
- Casabianca, L. B., Mohr, D., Mandal, S., Song, Y.-Q. & Frydman, L. Chirped CPMG for well-logging NMR applications. *J. Magn. Reson.* **242**, 197–202 (2014).
- Hennig, J., Nauerth, A. & Friedburg, H. RARE imaging: a fast imaging method for clinical MR. *Magn. Reson. Med.* **3**, 823–833 (1986).
- Casanova, F., Perlo, J., Blümich, B. & Kremer, K. Multi-echo imaging in highly inhomogeneous magnetic fields. *J. Magn. Reson.* **166**, 76–81 (2004).
- McDaniel, P. C., Cooley, C. Z., Stockmann, J. P. & Wald, L. L. The MR Cap: a single-sided MRI system designed for potential point-of-care limited field-of-view brain imaging. *Magn. Reson. Med.* **82**, 1946–1960 (2019).
- Hennig, J. et al. Parallel imaging in non-bijective, curvilinear magnetic field gradients: a concept study. *Magn. Reson. Mater. Phys.* **21**, 5–14 (2008).
- Stockmann, J. P., Ciris, P. A., Galiana, G., Tam, L. & Constable, R. T. O-space imaging: highly efficient parallel imaging using second-order nonlinear fields as encoding gradients with no phase encoding. *Magn. Reson. Med.* **64**, 447–456 (2010).
- Fessler, J. A. Model-based image reconstruction for MRI. *IEEE Signal Process. Mag.* **27**, 81–89 (2010).
- Schultz, G. et al. Reconstruction of MRI data encoded with arbitrarily shaped, curvilinear, nonbijective magnetic fields. *Magn. Reson. Med.* **64**, 1390–1403 (2010).
- Lin, F.-H. et al. Reconstruction of MRI data encoded by multiple nonbijective curvilinear magnetic fields. *Magn. Reson. Med.* **68**, 1145–1156 (2012).
- Heye, T. et al. The energy consumption of radiology: energy- and cost-saving opportunities for CT and MRI operation. *Radiology* **295**, 593–605 (2020).
- Srinivas, S. A., Cooley, C. Z., Stockmann, J. P., McDaniel, P. C. & Wald, L. L. Retrospective electromagnetic interference mitigation in a portable low field MRI system. *Proc. Intl Soc. Mag. Reson. Med.* **28**, 1269 (2020).
- Rearick, T., Charvat, G. L., Rosen, M. S. & Rothberg, J. M. Noise suppression methods and apparatus. US patent US9797971B2 (2017).
- Stockmann, J., McDaniel, P., Vaughn, C., Cooley, C. Z. & Wald, L. L. Feasibility of brain pathology assessment with diffusion imaging on a portable scanner using a fixed encoding field. *Proc. Intl Soc. Mag. Reson. Med.* **27**, 1196 (2019).
- Cooley, C. Z., McDaniel, P. C., Stockmann, J. P., Mateen, F. J. & Wald, L. L. Single-sided magnet design for an MR guided lumbar puncture (LP) device. *Proc. Intl Soc. Mag. Reson. Med.* **28**, 1266 (2020).
- McDaniel, P., Cooley, C. Z., Stockmann, J. P. & Wald, L. L. 3D imaging with a portable MRI scanner using an optimized rotating magnet and gradient coil. *Proc. Intl Soc. Mag. Reson. Med.* **26**, 0029 (2018).
- Bringout, G., Gräfe, K. & Buzug, T. M. Performance of shielded electromagnet—evaluation under low-frequency excitation. *IEEE Trans. Magn.* **51**, 1–4 (2015).
- Arango, N., Stockmann, J. P., Witzel, T., Wald, L. L. & White, J. Open-source, low-cost, flexible, current feedback-controlled driver circuit for local  $B_0$  shim coils and other applications. *Proc. Intl Soc. Mag. Reson. Med.* **24**, 1157 (2016).
- LaPierre, C., Sarracanie, M., Waddington, D. E. J., Rosen, M. S. & Wald, L. L. A single channel spiral volume coil for in vivo imaging of the whole human brain at 6.5 mT. *Proc. Intl Soc. Mag. Reson. Med.* **23**, 1793 (2015).
- Anand, S., Stockmann, J. P., Wald, L. L. & Witzel, T. A low-cost (<\$500 USD) FPGA-based console capable of real-time control. *Proc. Intl Soc. Mag. Reson. Med.* **26**, 0948 (2018).
- Blücher, C. et al. COSI transmit: open source soft- and hardware transmission system for traditional and rotating MR. *Proc. Intl Soc. Mag. Reson. Med.* **25**, 0184 (2017).
- Kunz, D. Frequency-modulated radiofrequency pulses in spin-echo and stimulated-echo experiments. *Magn. Reson. Med.* **4**, 129–136 (1987).
- Carr, H. Y. & Purcell, E. M. Effects of diffusion on free precession in nuclear magnetic resonance experiments. *Phys. Rev.* **94**, 630–638 (1954).

### Acknowledgements

We thank T. Witzel for valuable advice over the course of developing the system, as well as specific assistance with consoles; M. Haskell for contributing to the magnet design algorithm; M. David for assistance with the gradient nonlinearity analysis; S. Sigalovsky for the construction of mechanical components; J. Conklin for insightful discussions on clinical applications; and N. Koonjoo for help with the helmet coil design. The research reported in this publication was supported by the National Institute of Biomedical Imaging and Bioengineering of the National Institutes of Health under award nos. R01EB018976, 5T32EB1680 and R00EB021349.

### Author contributions

C.Z.C., P.C.M., J.P.S., S.A.S., C.R.S., C.F.V., M.S., M.S.R. and L.L.W. contributed to or advised on system design, implementation and validation experiments. C.Z.C., J.P.S., S.F.C. and B.G. contributed to development of the image reconstruction method. M.H.L. provided guidance for clinical application and subsequent design choices. C.Z.C. wrote the manuscript. All authors contributed to reviewing and editing the manuscript.

### Competing interests

M.H.L. is a consultant for GE Healthcare and receives research funding from GE Healthcare. L.L.W. and S.F.C. receive research funding from Siemens Healthineers. M.S.R. is a co-founder of Hyperfine Research and receives research funding from GE Healthcare. C.Z.C., J.P.S. and L.L.W. are listed as inventors on a patent (US patent 10,359,481) filed by Partners HealthCare for portable MRI using a rotating array of permanent magnets. C.Z.C., J.P.S., B.G., M.S.R. and L.L.W. are listed as inventors on a patent (US patent application 16/092,686) filed by Partners HealthCare for the use of swept RF pulses applied with RF spatial phase gradients. C.Z.C., J.P.S. and L.L.W. are consultants and equity holders for Neuro42, Inc.

### Additional information

**Supplementary information** is available for this paper at <https://doi.org/10.1038/s41551-020-00641-5>.

**Correspondence and requests for materials** should be addressed to C.Z.C.

**Peer review information** Peer reviewer reports are available.

**Reprints and permissions information** is available at [www.nature.com/reprints](http://www.nature.com/reprints).

**Publisher's note** Springer Nature remains neutral with regard to jurisdictional claims in published maps and institutional affiliations.

© The Author(s), under exclusive licence to Springer Nature Limited 2020



## Reporting Summary

Nature Research wishes to improve the reproducibility of the work that we publish. This form provides structure for consistency and transparency in reporting. For further information on Nature Research policies, see our [Editorial Policies](#) and the [Editorial Policy Checklist](#).

### Statistics

For all statistical analyses, confirm that the following items are present in the figure legend, table legend, main text, or Methods section.

n/a Confirmed

- The exact sample size ( $n$ ) for each experimental group/condition, given as a discrete number and unit of measurement
- A statement on whether measurements were taken from distinct samples or whether the same sample was measured repeatedly
- The statistical test(s) used AND whether they are one- or two-sided  
*Only common tests should be described solely by name; describe more complex techniques in the Methods section.*
- A description of all covariates tested
- A description of any assumptions or corrections, such as tests of normality and adjustment for multiple comparisons
- A full description of the statistical parameters including central tendency (e.g. means) or other basic estimates (e.g. regression coefficient) AND variation (e.g. standard deviation) or associated estimates of uncertainty (e.g. confidence intervals)
- For null hypothesis testing, the test statistic (e.g.  $F$ ,  $t$ ,  $r$ ) with confidence intervals, effect sizes, degrees of freedom and  $P$  value noted  
*Give  $P$  values as exact values whenever suitable.*
- For Bayesian analysis, information on the choice of priors and Markov chain Monte Carlo settings
- For hierarchical and complex designs, identification of the appropriate level for tests and full reporting of outcomes
- Estimates of effect sizes (e.g. Cohen's  $d$ , Pearson's  $r$ ), indicating how they were calculated

*Our web collection on [statistics for biologists](#) contains articles on many of the points above.*

### Software and code

Policy information about [availability of computer code](#)

- |                 |   |
|-----------------|---|
| Data collection | MRI data collection was performed with TNMR Version 3.4.31 software provided with the Tecmag Bluestone console (Houston, TX, USA). Magnetic field-mapping data were collected using custom code in MATLAB 2018b (Natick, MA, USA) and via appropriate interfacing with the 3-axis magnetometer (THM1176, MetroLabs, Geneva, Switzerland) and motion controller (SMC6480, Leadshine America Inc., Foothill Ranch, CA, USA). Field-mapping MATLAB code and TNMR files are available from the corresponding author upon request. |
| Data analysis   | MRI data were analysed with custom code in MATLAB 2018b. Image-reconstruction and processing code and exemplary data are available in github at <a href="https://github.com/czcooley/portable-MRI">https://github.com/czcooley/portable-MRI</a> .   |

For manuscripts utilizing custom algorithms or software that are central to the research but not yet described in published literature, software must be made available to editors and reviewers. We strongly encourage code deposition in a community repository (e.g. GitHub). See the Nature Research [guidelines for submitting code & software](#) for further information.

### Data

Policy information about [availability of data](#)

All manuscripts must include a [data availability statement](#). This statement should provide the following information, where applicable:

- Accession codes, unique identifiers, or web links for publicly available datasets
- A list of figures that have associated raw data
- A description of any restrictions on data availability

The main data supporting the results in this study are available within the paper and its Supplementary Information. All reconstructed MATLAB image files and one exemplary raw dataset are available in github at <https://github.com/czcooley/portable-MRI>.

## Field-specific reporting

Please select the one below that is the best fit for your research. If you are not sure, read the appropriate sections before making your selection.

Life sciences       Behavioural & social sciences       Ecological, evolutionary & environmental sciences

For a reference copy of the document with all sections, see [nature.com/documents/nr-reporting-summary-flat.pdf](https://www.nature.com/documents/nr-reporting-summary-flat.pdf)

## Life sciences study design

All studies must disclose on these points even when the disclosure is negative.

Sample size	Following phantom studies (not shown), three human subjects were scanned with the portable MRI scanner to demonstrate the qualitative imaging capabilities of the scanner. A grapefruit was also imaged to demonstrate imaging in a different structural sample. The SNR of each image was calculated as the mean of a high intensity ROI (~30 voxels) divided by the mean standard deviation of background ROI (~800 voxels).
Data exclusions	Some human-subject data were excluded owing to incorrect subject positioning in the scanner.
Replication	Imaging results were highly replicable in phantoms. Phantom-imaging experiments were performed more than 20 times. Differences in human-subject anatomy, size and positioning were reflected in human-subject imaging.
Randomization	Randomization was not applicable, as the goal of the study was qualitative image validation with the portable MRI device.
Blinding	Blinding was not relevant to the study, as the goal was qualitative image validation with the portable MRI device. Subject data were anonymised for protection, as per HIPAA rules.

## Reporting for specific materials, systems and methods

We require information from authors about some types of materials, experimental systems and methods used in many studies. Here, indicate whether each material, system or method listed is relevant to your study. If you are not sure if a list item applies to your research, read the appropriate section before selecting a response.

### Materials & experimental systems

n/a	Involved in the study
<input checked="" type="checkbox"/>	<input type="checkbox"/> Antibodies
<input checked="" type="checkbox"/>	<input type="checkbox"/> Eukaryotic cell lines
<input checked="" type="checkbox"/>	<input type="checkbox"/> Palaeontology and archaeology
<input checked="" type="checkbox"/>	<input type="checkbox"/> Animals and other organisms
<input type="checkbox"/>	<input checked="" type="checkbox"/> Human research participants
<input checked="" type="checkbox"/>	<input type="checkbox"/> Clinical data
<input checked="" type="checkbox"/>	<input type="checkbox"/> Dual use research of concern

### Methods

n/a	Involved in the study
<input checked="" type="checkbox"/>	<input type="checkbox"/> ChIP-seq
<input checked="" type="checkbox"/>	<input type="checkbox"/> Flow cytometry
<input type="checkbox"/>	<input checked="" type="checkbox"/> MRI-based neuroimaging

## Human research participants

Policy information about [studies involving human research participants](#)

Population characteristics	The MRI subjects were healthy volunteers. Male and female subjects of age 18 to 65 were recruited.
Recruitment	The patients were recruited by investigators at Massachusetts General Hospital. There were no self-selection biases or other biases.
Ethics oversight	The study was approved by the Partners Healthcare Institutional Review Board (IRB), and written informed consent was obtained prior to the examination.

Note that full information on the approval of the study protocol must also be provided in the manuscript.

## Magnetic resonance imaging

### Experimental design

Design type      Structural neuroimaging

Design specifications	T2-weighted, T1-weighted, and proton density (PD) structural images were acquired in phantoms, fruit, and human subjects. No performance/task-based/resting-state fMRI or clinical trials were performed.
Behavioral performance measures	No behavioral tasks were performed.

## Acquisition

Imaging type(s)	Structural neuroimaging
Field strength	80 mT
Sequence & imaging parameters	3D RARE-based (spin echo) pulse sequences were used. The acquisition field of view was 32 cm x 22 cm x 16 cm, and matrix size was 256 x 97 x 23. PD images were acquired with a 3D RARE, TR/TEeff = 2900ms / 14ms. T1-weighted images were acquired with an inversion prepped 3D RARE, TI/TR/TEeff = 400ms / 1830ms / 14ms. T-2-weighted images were acquired with a 3D RARE sequence, TR/TEeff = 3000ms / 167ms.
Area of acquisition	Brain
Diffusion MRI	<input type="checkbox"/> Used <input checked="" type="checkbox"/> Not used

## Preprocessing

Preprocessing software	MATLAB 2018b was used to process the imaging data.
Normalization	The images were processed with a custom 'intensity correction' MATLAB script that corrects for the intensity difference of the partitions due to B1 inhomogeneity.
Normalization template	No normalization template was used.
Noise and artifact removal	Masked areas in a 22 cm x 18 cm FOV are reconstructed using the described generalized reconstruction method that corrects for geometric distortion using measured field maps. This was implemented with custom MATLAB image-reconstruction code.
Volume censoring	Custom image masks around the subjects' head were used in MATLAB.

## Statistical modeling & inference

Model type and settings	No statistical modelling and inference were used.
Effect(s) tested	No tasks or stimulus effects were tested.
Specify type of analysis:	<input type="checkbox"/> Whole brain <input type="checkbox"/> ROI-based <input type="checkbox"/> Both
Statistic type for inference (See <a href="#">Eklund et al. 2016</a> )	No statistical modelling and inference were used.
Correction	No statistical modelling and inference were used.

## Models & analysis

n/a	Involved in the study
<input checked="" type="checkbox"/>	<input type="checkbox"/> Functional and/or effective connectivity
<input checked="" type="checkbox"/>	<input type="checkbox"/> Graph analysis
<input checked="" type="checkbox"/>	<input type="checkbox"/> Multivariate modeling or predictive analysis